JOURNAL OF SPACECRAFT AND ROCKETS
Vol. 46, No. 2, March–April 2009

Supersonic Inflatable Aerodynamic Decelerators for Use on Future Robotic Missions to Mars

Ian G. Clark,* Allison L. Hutchings,* Christopher L. Tanner,* and Robert D. Braun†
Georgia Institute of Technology, Atlanta, Georgia 30332-0150

DOI: 10.2514/1.38562

The potential advantages of using a supersonic inflatable aerodynamic decelerator were analyzed for a notional 2016 Mars robotic mission. Two inflatable decelerator configurations, the attached isotensoid decelerator and the tension cone, were sized and traded against their system-level performance impact. The analyses included preliminary aerodynamic drag estimates for the different configurations, insight into the entry trajectory advantages provided, and preliminary geometric and mass estimates for the decelerator systems. The attached isotensoid configuration was calculated to have a lower drag but a slightly lighter mass solution vs the tension cone. Both devices showed an excellent capability of decelerating entry vehicles at significantly higher altitudes than is currently possible with the traditional supersonic parachute. The configurations analyzed demonstrated a relative insensitivity to a 25% increase in entry mass. Large increases in payload mass capability were calculated as a function of the conditions at which the inflatable decelerator staged to a propulsive terminal descent system.

Nomenclature

A	=	area, m^2
C	=	force coefficient
c	=	scaling factor required to meet a material constraint
D	=	drag
E	=	modulus of elasticity
g_0	=	acceleration due to Earth's gravity
I	=	moment of inertia, or impulse
l	=	length, m
k	=	factor of safety
M	=	Mach number
m	=	mass, kg
N	=	stress resultant, N/m
n	=	number of meridional cords
r	=	radius, m
P	=	hoop force
p	=	pressure, N/m^2
q	=	dynamic pressure, N/m^2
R	=	specific gas constant, J/kg-K
T	=	tension, N/m^2
t	=	thickness, m
V	=	volume, m^3
w	=	width, m
β	=	decelerator ballistic coefficient
Γ	=	portion of burble fence load carried by fabric
γ	=	relative flight-path angle, deg
ρ	=	areal density, kg/m^2

Subscripts

a	=	aeroshell
b	=	base
c	=	canopy
cr	=	critical
D	=	drag
f	=	front or windward
i	=	internal or initial
iso	=	isotensoid
m	=	meridian
p	=	parachute
pl	=	payload
prop	=	propellant
r	=	rear or leeward
t	=	torus
tc	=	tension cone
ts	=	tension shell
0	=	torus/tension shell interface
α	=	maximum isotensoid height
θ	=	circumferential direction
ϕ	=	meridional direction
∞	=	freestream condition

Presented at the 2008 IEEE Aerospace Conference, Big Sky, MT, 1–8 March 2008; received 14 May 2008; revision received 20 August 2008; accepted for publication 25 August 2008.

*Graduate Research Assistant, Guggenheim School of Aerospace Engineering. Student Member AIAA.

†Associate Professor, Guggenheim School of Aerospace Engineering. Fellow AIAA.

I. Introduction

TOWARD the end of the 1960s, NASA began several technology development programs aimed at maturing deceleration technologies for use in thin-atmosphere entries. Research into entry body shapes and supersonic parachutes was undertaken with the objective of enabling the successful landing of a spacecraft on the surface of Mars. Although the initial beneficiaries of these efforts were the two 590 kg Viking landers, the developed technologies became the foundation for every subsequent Mars entry vehicle. Over the past 30 years, incremental improvements in aeroshell and parachute technologies have allowed for a gradual increase in Mars landed mass. However, these improvements are rapidly reaching their limits. The latest mission in development, the 2009 Mars Science Laboratory (MSL), is being designed to land an 850 kg rover at an altitude of at least 1 km [1]. To do this, the MSL will require the largest diameter aeroshell (4.5 m) and the largest diameter supersonic parachute (21.5 m) ever flown on Mars (see Table 1). Furthermore, parachute deployment is planned at a higher Mach number (2.2) and dynamic pressure (750 Pa) [2,3] than on any previous Mars mission. This system may be near the limits of current parachute technology [4], and later missions attempting marginal increases in landed mass will be faced with a difficult decision: either attempt to extrapolate current decelerator technology further beyond the tested and validated flight regime or invest in a new, costly technology development program.

One promising technology path involves the use of a supersonic inflatable aerodynamic decelerator (IAD). Often referred to as

Table 1 Supersonic DGB dimensions and nominal deployment conditions

Mission	Diameter, m	Area, m^2	Deployment Mach number	Deployment Q, Pa	Landed mass, kg
Viking I	16.0	201.1	1.1	350	612
Viking II	16.0	201.1	1.1	350	612
MPF	12.5	122.7	1.57	585	370
MER-A	14.0	153.9	1.77	725	539
MER-B	14.0	153.9	1.77	750	539
Phoenix	11.7	107.5	1.2	430	364
MSL	21.5	363.1	2.2	750	850
AFL/MSR	23.0	415.5	2.3	800	∼1050

"ballutes" in the literature, IADs underwent a considerable amount of development beginning in the late 1960s [4]. This included the derivation of fundamental structural theories [5], several sets of wind-tunnel tests [6], and multiple atmospheric flight tests [7] on a variety of configurations. However, because the impetus for much of the initial research was as a parallel technology path for the Viking decelerator program, development effectively ended with that program's conclusion. More recently, NASA's Program to Advance Inflatable Decelerators for Atmospheric Entry (PAIDAE) has begun a development program aimed at maturing IADs for both human and robotic use. Areas of focus for PAIDAE include material development, mission and system design, wind-tunnel testing, and atmospheric flight testing of deployable aerodynamic decelerators.

The primary purpose of a supersonic IAD is to provide a large drag area at Mach numbers and dynamic pressures considerably higher than those presently possible using parachutes. This earlier deployment provides several distinct advantages, including an increased time line for key staging events, deceleration at higher altitudes, and access to higher-elevation landing sites. Although hypersonic IADs offer additional benefits in the form of reduced heating rates, supersonic IADs provide a more near-term technology solution to the problem of landing 1 t and larger masses on the surface of Mars. Furthermore, the development of supersonic IADs would set the groundwork for the eventual qualification of IADs for hypersonic use.

The objective of this investigation is to quantify the potential advantages offered by a supersonic IAD with respect to a baseline robotic Mars mission. Preliminary aerodynamic and structural analyses are conducted for two separate IAD configurations. Results from these analyses are used to quantify trajectory effects and provide mass estimates for an IAD system. Finally, key sensitivities are addressed so as to provide insight into areas of further research and technology development.

II. Mission Overview

A. Nominal Mission

A large rover mission in the 2016 Mars opportunity is used as the baseline for this investigation. Such a mission may take shape through either the Astrobiology Field Laboratory (AFL) or the Mars Sample Return (MSR) flight projects. Envisioned as a follow-on rover mission to the MSL, a significant portion of the MSL entry, descent, and landing heritage is assumed [8]. The entry vehicle configuration, shown in Fig. 1, is identical to that used by the MSL. The rover mass is anticipated to be 10–25% higher than the MSL, primarily due to accommodation of a more complex science payload [8] and increased pinpoint landing requirements. For the purposes of this study, an entry mass of 4200 kg is assumed (31% higher than the MSL). It should be noted that this value yields a packing density of approximately 195 kg/m^3, or nearly 85% of the packing density achieved with the Mars exploration rovers, implying a complex and difficult packaging arrangement.

The 2016 mission entry sequence is intended to mirror the MSL in many respects, including the use of a center of mass offset to provide trim at an angle of attack and subsequently an L/D of approximately 0.24. Hypersonic guidance via lift vector (bank-angle) modulation is used as the baseline to improve landing accuracy. In the present study, a reference trajectory is assumed using a reference bank-angle profile, an entry flight-path angle of −16.1 deg, and an entry velocity of 5.2 km/s. The resulting trajectory is shown in Fig. 2.

For this reference trajectory, the final stages of descent assume nominal deployment of a 23 m supersonic disk-gap-band (DGB) parachute at a Mach number of 2.3 and a dynamic pressure of 800 Pa. Note that this assumed DGB parachute performance is better than that planned for the MSL, which itself is above that successfully demonstrated to date (see Table 1). Upon inflation, the parachute rapidly decelerates the entry vehicle through transonic and into subsonic flight conditions. As with the MSL, heat shield separation is assumed to occur upon reaching a Mach number of 0.7. The terminal descent portion of the flight is performed using the MSL Sky Crane architecture. For the MSL, powered descent initiation is dependent upon ground acquisition by a terminal descent sensor followed by a measurement of the vehicle's altitude and velocity [1]. Although no specific set of flight conditions define the point at which the descent engines are ignited, it was assumed that the earliest this event could occur is 20 s after heat shield jettison. For the reference trajectory, this occurs at an altitude of 7.3 km and a velocity of 112 m/s.

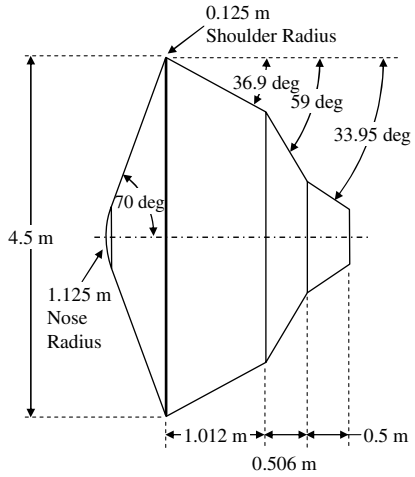

Fig. 1 AFL entry capsule.

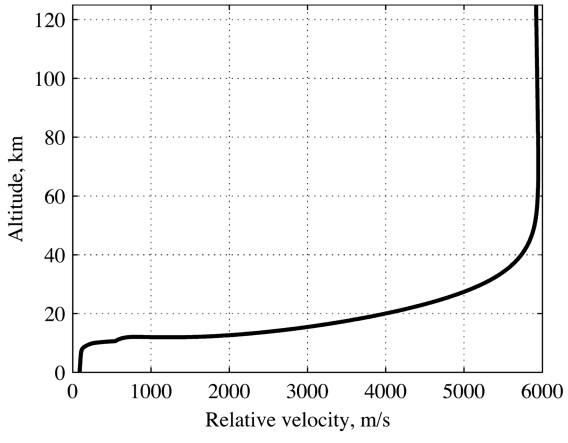

Fig. 2 Reference trajectory.

B. Inflatable Aerodynamic Decelerator Modified Mission

Two major variations to the reference mission profile are proposed. The first consists of the elimination of the DGB parachute in favor of a supersonic inflatable aerodynamic decelerator. The objective in this case is to allow for significant deceleration earlier in the trajectory and, consequently, landing at higher elevations than would otherwise be possible using a parachute alone.

Previous robotic Mars missions have limited parachute deployment to Mach numbers of less than 2.1 due to the lack of deployment and initial inflation test data obtained at the Earth in Mars-relevant conditions above this Mach number and the severe area oscillations that have been observed in DGB parachutes at Mach numbers above approximately 1.5. Historical testing of supersonic IADs has shown no area oscillation susceptibility due to Mach number effects. Thus, this analysis placed no such Mach restriction with the exception that deployment must occur at a Mach number of less than 5 to allow the neglect of aerothermal heating considerations.

By design of the reference bank profile, as the entry vehicle slows to supersonic velocities, the lift vector is returned to near vertical, causing a small loft in the trajectory. The IAD-modified mission takes advantage of this feature by waiting until the peak loft altitude is attained before initiating deployment. Entry flight-path angle variation was also performed in an attempt to position this loft at Mach numbers and altitudes larger than for the nominal trajectory.

C. Two-Stage Inflatable Aerodynamic Decelerator/Parachute Mission

Although IADs offer excellent aerodynamics in high-Mach-number, high-dynamic-pressure environments, this generally comes at the expense of a system that is more massive than a traditional parachute. Parachutes, on the other hand, perform very well in subsonic environments. Previous studies have shown that the optimal solution from a mass standpoint may be to incorporate a two-stage IAD/parachute system [9]. In this manner, the IAD can be deployed at high supersonic conditions, decelerate the vehicle to subsonic conditions, and then give way to a more efficient parachute system. The second alternative mission profile examines this concept by discarding the IAD at a Mach number of 0.9 and subsequently deploying a ringsail parachute.

III. Decelerator Configurations

Three types of aerodynamic decelerators are evaluated for this study: a supersonic tension cone IAD, a supersonic isotensoid IAD, and a subsonic ringsail parachute. Descriptions of each are provided below.

A. Tension Cone

The tension cone concept consists of a shell of revolution that is inherently shaped so as to contain only tensile stresses. The shape of the shell is derived from a prescribed pressure distribution using linear membrane theory [5]. The tension in the shell is resisted at one end by attachment to the entry vehicle and at the other end by the use of a compression ring, typically consisting of an inflated torus. A conceptual image of the tension shell as it is envisioned for this study is provided Fig. 3.

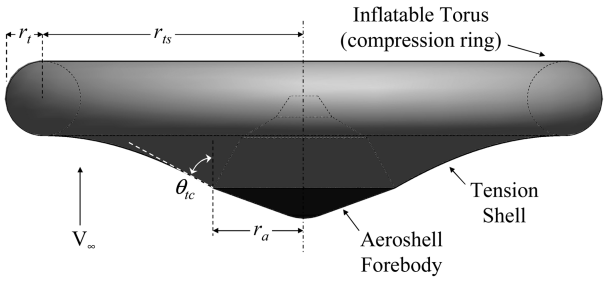

Fig. 3 Tension cone configuration.

Table 2 Baseline tension cone geometry values

Parameter	Value
Cone angle, θ_{tc}	60 deg
Ratio of tension cone area to aeroshell area, $(r_{ts}/r_t)^2/r_a^2$	10
Torus radius ratio, r_{ts}/r_t	7
r_a	2.25 m
r_{ts}	6.225 m
r_t	0.89 m

For later aerodynamic analyses, a baseline tension cone configuration was established. The primary geometric parameters for the baseline tension cone are provided in Table 2. The exact shape of the tension shell portion was determined by the iteration of inviscid computational fluid dynamics (CFD) solutions. The iteration consisted of calculating an initial curvature assuming a Newtonian pressure distribution. Subsequent CFD analysis on the Newtonian-derived shell provided a new pressure distribution, which, in turn, was used to calculate a new shell shape. Three additional iterations yielded a converged shape.

Deployment of the tension cone occurs when the torus is rapidly pressurized using either a gas generator or pressure-tank-based inflation system. Detailed modeling of the inflation system and deployment dynamics are neglected for this conceptual design study.

B. Isotensoid Decelerator

The Attached Inflatable Decelerator (AID) was developed in the late 1960s by the Goodyear Aerospace Corporation to overcome flutter and stability problems encountered with supersonic parachutes. The concept consists of an aftbody decelerator that is directly attached to the aeroshell. The AID was designed using isotensoid theory [10], which provides constant tension along the decelerator's meridional cords and uniform fabric stress in all directions throughout the surface. Designing for uniform fabric stress prevents the formation of local wrinkles along the decelerator surface (which have been shown to cause undesirable flutter and structural failure) and results in easier fabrication than other concepts with varying stress.

The AID uses ram-air inlets, shown in Fig. 4, that face the direction of the local flow to maintain the canopy shape and create an internal pressure greater than that of the external aerodynamic pressure. Additionally, a burble fence, located at the maximum radius of the isotensoid, is employed to add aerodynamic stability at transonic and subsonic speeds. The AID used in this study is shown in Fig. 5 with the pertinent isotensoid parameters indicated in Table 3. Similar to the tension cone, the decelerator canopy half-angle (θ_{iso}) does not precisely match the aeroshell half-angle (θ_a) at the attach point.

The inflation rate of the AID is a function of the mass flow rate into the canopy through the ram-air inlets and out of the canopy due to material porosity. These rates can be tailored by optimizing the inlet area and material porosity to achieve a desired inflation rate that

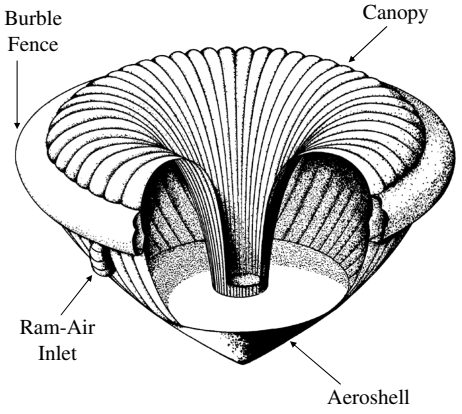

Fig. 4 Illustration of AID concept [6].

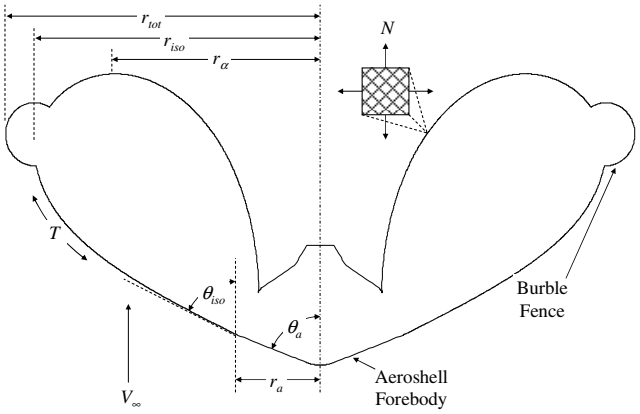

Fig. 5 AID configuration schematic.

balances deceleration loads and inflation stability. Wind-tunnel testing of the inflation process indicated inflation times on the order of 0.6 s for a 1.5-m-diam device [11]. Inflation times for full-scale articles are expected to be of a similar order; thus, inflation of the AID device is modeled as instantaneous.

C. Ringsail Parachute

A ringsail parachute was analyzed as a potential second-stage decelerator as it has demonstrated a high subsonic drag coefficient and good stability characteristics and is relatively lightweight per unit drag area [12]. Additionally, the ringsail canopy can be designed for optimum performance for a given flight condition, enabling ringsail configurations to achieve subsonic drag coefficients of 0.8 or better.

Subsonic inflation of the parachute can be modeled as occurring linearly over a constant number of parachute diameters [12]. Even for a large (>20-m-diam) parachute deploying at 100 m/s, the inflation time is less than 2 s; thus, in this analysis, the ringsail parachute inflation is also modeled as occurring instantaneously.

IV. Aerodynamics

A moderate amount of wind-tunnel testing of the two IAD configurations was performed in the 1960s [6,11,13]. This included an evaluation of the deployment behavior of several isotensoid models as well as a static aerodynamic characterization of the isotensoid and tension cone concepts.

The results from the isotensoid deployment tests demonstrated favorable behavior, including the lack of any flutter characteristics [11]. Additionally, the isotensoid shape did not exhibit shock loads commonly observed in parachute deployments. Possible explanations for this include the lack of an apparent mass effect and the ram-air inflation mechanism providing a more controlled deployment. Drag coefficients measured at supersonic conditions were typically between 1.1 and 1.2, though models tested without the burble fence provided slightly higher values of about 1.4. Drag was observed to vary little, with minor variations in the angle of attack and Reynolds number [11].

The testing of multiple rigid tension cone configurations yielded drag coefficients between 1.3 and 1.6 depending upon cone angle (θ_{tc}), nose radius, and shoulder radius (r_t). Of particular interest due to aerothermal and stability concerns was the presence of embedded shocks on the tension shell depending upon the cone angle. In particular, shallow and moderate cone angles at an angle of attack demonstrated embedded shocks [13].

Table 3 AID parameters

Parameter	Symbol	Dimension
Total decelerator radius	r_{tot}	$1.1r_{iso}$
Aeroshell attach point radius	r_a	$0.2985r_{iso}$
Radius at max. isotensoid height	r_α	$0.70r_{iso}$
Aeroshell half-angle	θ_a	70 deg
Leeward fabric stress resultant	N_r	900 N/m

An aerodynamic assessment of the two IAD configurations was performed for the purpose of establishing an approximate aerodynamic data set for trajectory modeling. Using the wind-tunnel data as a source of validation, a computational analysis of the baseline geometries was performed. NASCART-GT, a Cartesian-grid-based CFD code [14], was used to analyze the baseline IAD configurations. Cases were run at a 0 deg angle of attack across a range of nominal trajectory points to provide profiles of the drag coefficient as a function of Mach number. Supersonic cases assumed inviscid aerodynamics and demonstrated good agreement with the wind-tunnel data. Transonic and subsonic cases were run using the Navier–Stokes analysis capability of NASCART-GT.

Sample results from the analysis are shown in Figs. 6 and 7. In the case of the tension cone, the CFD analysis confirmed that the 60 deg cone angle was sufficient to prevent the formation of an embedded shock on the tension shell surface. However, the isotensoid configuration exhibited a weak shock forming just in front of the burble fence. Although the literature lacks schlieren imagery from the wind-tunnel tests of the isotensoid, it is expected that an embedded shock likely existed in those tests as well. Video imagery from some of those tests showed no detrimental impact on the IAD or the burble fence due to flow separation behind the embedded shock.

The computational aerodynamic analysis was compiled into a preliminary aerodynamic database of the two baseline IAD configurations. These results are shown in Fig. 8. From the results it can be seen that the tension cone offers similar drag performance to a rigid 60 or 70 deg sphere cone whereas the isotensoid configuration provides roughly 20% less drag. Furthermore, neither IAD configuration exhibits the transonic drag bucket common to parachutes and other decelerators that trail an entry system. The lack of a drag bucket may allow for the heat shield to be discarded much

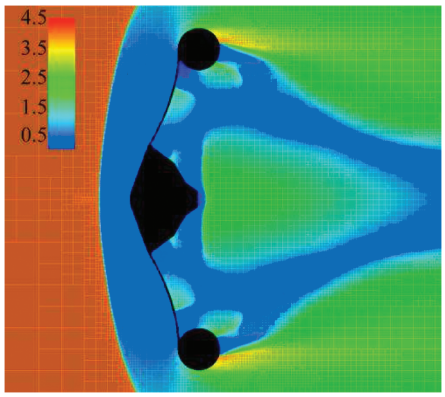

Fig. 6 Inviscid Mach number profile for the baseline tension cone configuration at Mach 4.5.

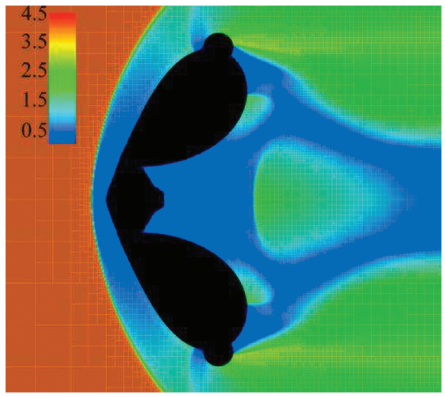

Fig. 7 Inviscid Mach number profile for the baseline isotensoid configuration at Mach 4.5.

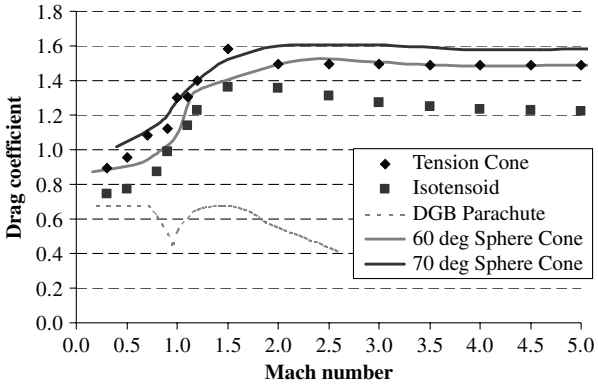

Fig. 8 Comparison of the drag coefficient as a function of Mach number for IADs, sphere cone aeroshells, and parachutes.

earlier in the trajectory, as recontact with the entry vehicle is less likely.

V. Structural Analysis

Neither the tension cone decelerator nor the isotensoid decelerator has been fabricated at a scale comparable to flightlike devices. Thus, many uncertainties exist about the exact nature in which these articles would be fabricated. These uncertainties, in turn, make mass estimation difficult. For this study, an approach was used in which basic structural principles were combined with tension cone and isotensoid shape theory. The result was a preliminary estimate of the loads and stresses encountered by the two supersonic IADs. This, in turn, was combined with assumed material properties to derive thickness estimates and subsequently material mass estimates. A summary of the structural considerations incorporated in the analysis is provided below.

A. Tension Cone Structural Analysis

The inflatable tension cone consists of two elements, the tension shell and the inflated torus. The tension shell provides a majority of the drag area whereas the torus is used to resist the loading of the tension shell. The meridional stress resultant $N_{\phi,\mathrm{ts}}$, expressed in Eq. (1), is a function of the drag felt by the shell (D_{ts}) and the torus (D_t), the shell attachment angle (θ_{tc}), and the aeroshell radius (r_a) [5]:

$$N_{\phi,\mathrm{ts}} = \frac{D_t + D_{\mathrm{ts}}}{2\pi r_a \sin\theta_{\mathrm{tc}}} \tag{1}$$

The key structural constraint for the tension shell is that the meridional stress resultant ($N_{\phi,\mathrm{ts}}$) does not exceed the yield strength of the shell material, $N^{\max}_{\phi,\mathrm{ts}}$, such that

$$\frac{N_{\phi,\mathrm{ts}}}{c_{\mathrm{ts}}} \le N^{\max}_{\phi,\mathrm{ts}} \tag{2}$$

where c_{ts} is the scaling factor required to meet the constraint of the tension shell material. The use of Eqs. (1) and (2) allows for an estimate of the necessary increase in strength of the allowable material stress resultants ($N^{\max}_{\phi,\mathrm{ts}}$), which can be achieved by using more layers of fabric or a stronger material. That is, often the yield strength of a material is provided for a given thickness of the material. In that case, the required thickness is attained by multiplying the nominal (provided) material thickness by the scaling factor c_{ts} such that Eq. (2) is satisfied.

The primary sources of stress on the inflatable torus originate from the tension shell loading and the internal pressure required to resist that loading. Five design constraints were identified for the torus, three stress-based criteria and two planar buckling criteria. These include the following:

1) The compressive meridional stress resultant on the torus must be less than the maximum material strength ($N^{\max}_{\phi,t}$):

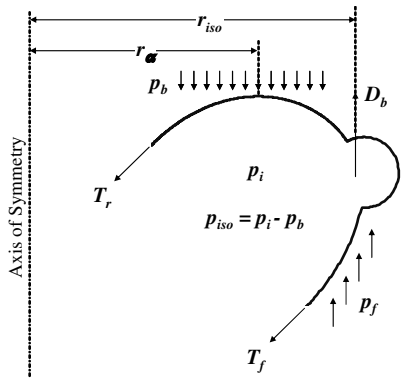

Fig. 9 AID structural parameters.

$$N_{\phi,t} = -\frac{r_{\mathrm{ts}} N_o}{\pi r_t c_t} \le N^{\max}_{\phi,t} \tag{3}$$

where r_t and r_{ts} are defined in Fig. 3, t_t is the thickness of the torus material, and N_0 is the meridional stress resultant N_ϕ evaluated at the torus/tension shell interface ($N_o = r_a N_{\phi,\mathrm{ts}}/r_b$).

2) The inflation pressure must be sufficient to prevent local wrinkling on the torus walls from the compressive stress. The stress resultant in compression [Eq. (3)] and the counteracting tensile stress resultant due to the internal pressure of a toroidal shell [15] can be balanced to solve for the necessary pressure:

$$p_t \ge \frac{2 r_{\mathrm{ts}} N_o}{\pi r_t^2} \tag{4}$$

3) The torus stress resultant in the circumferential direction (N_{θ,p_t}) must not exceed material limits [15]:

$$N_{\theta,p_t} = \frac{p_t r_t}{2c_t}\frac{2r_{\mathrm{ts}} - r_t}{r_{\mathrm{ts}} - r_t} \le N^{\max}_{\theta,p_t} \tag{5}$$

4) The applied hoop force due to the tension shell loading (P) must be lower than the force needed to induce *in-plane* buckling [16,17]:

$$P_{\mathrm{cr},i} = \frac{4.5EI}{r_b^2}\left(1 + \frac{3}{2}c + \frac{4 + 4.5c}{S + P^*}\right)^{-1} \tag{6}$$

$$P = \frac{D_{\mathrm{ts}}}{\cos\theta_{\mathrm{tc}}} \le P_{\mathrm{cr},i} \tag{7}$$

where E is the material's modulus of elasticity and I is the torus inertia tensor. The parameters c, S, and P^* are the shear stiffness, toroid slenderness, and pressure stiffness parameters defined in [17].

5) The applied force due to the tension shell loading must be lower than the force needed to induce *out-of-plane* buckling [16,17]:

$$P_{\mathrm{cr},o} = \frac{EI}{r_{\mathrm{ts}}^2}\left(12 + \frac{3}{2}\frac{\Gamma}{S + P^*}\right)\left[4 + 5c + \frac{1}{\Gamma}\left(1 + \frac{20}{3}c\right) + \frac{1}{S + P^*}\left(\frac{99}{8} + \frac{111}{8}c\right) + \frac{\Gamma}{S + P^*}\left(\frac{1}{2} + \frac{5}{6}c\right)\right]^{-1} \tag{8}$$

$$P = \frac{D_{\mathrm{ts}}}{\cos\theta_{\mathrm{tc}}} \le P_{\mathrm{cr},o} \tag{9}$$

where Γ is a buckling load parameter defined in [17].

A major assumption inherent in these formulations is that the torus wall is a membrane structure; thus, the local bending stiffness of the torus walls is neglected. This has particular implications in the determination of the required inflation pressure p_t and in the two buckling modes. Because of this assumption, the section stiffness (EI) is currently only affected by the material properties (E) and geometry (I). It should be noted that, for the cases investigated, the required pressures calculated using Eq. (4) were sufficiently high that

additional section stiffness was not needed to satisfy the buckling criteria. However, torus construction methods that provide additional stiffness other than that due to pressurization, such as those that incorporate stiffer materials or filament overwrapping, would likely reduce pressure requirements and provide an additional torus buckling margin.

B. Isotensoid Structural Analysis

Isotensoid design is based on equal principle forces in the fabric between meridians, which are constant over the canopy surface. Additionally, the tension in each meridian is constant over its entire length. For AID design, these principles hold except that the fabric stress and meridional tension is higher on the windward side due to the concentrated load of the burble fence at the canopy equator. The nondimensional fabric stress ($\bar{f}$) and meridional tension ($\bar{T}$) coefficients are given by Eqs. (10) and (11). The fabric stress is related to the meridional tension by the geometry of the isotensoid via Eq. (12).

$$\bar{f} = \frac{2f}{p_{\text{iso}} r_{\text{iso}}} \tag{10}$$

$$\bar{T} = \frac{nT}{p_{\text{iso}} \pi r_{\text{iso}}^2} \tag{11}$$

$$\bar{f} + \bar{T} = 1 - r_\alpha^2 \tag{12}$$

where f is the fabric stress resultant (in force per unit length), T is the meridional tension load, p_{iso} is the internal pressure minus the base pressure, r_{iso} is the equatorial radius of the isotensoid, n is the number of meridional cords, and r_α is a nondimensional parameter that defines the radius of maximum canopy height.

The windward fabric stress and meridional tension coefficients are assumed to take a fraction (Γ) of the burble fence load in addition to the leeward loading.

$$\bar{f}_f = \bar{f}_r + \Gamma \bar{N}_b \tag{13}$$

$$\bar{T}_f = \bar{T}_r + (1 - \Gamma)\bar{N}_b \tag{14}$$

$$\bar{N}_b = \frac{D_b}{p_{\text{iso}} \pi r_{\text{iso}}^2} \tag{15}$$

$$\Gamma = \frac{\bar{f}_r}{1 - r_\alpha^2} \tag{16}$$

where the subscripts f and r represent the front (windward) and rear (leeward) components, $\bar{N}_b$ is the nondimensional burble fence load, and D_b is the burble fence load. The isotensoid parameters specified are illustrated in Fig. 9. From these structural parameters and a choice of meridian and canopy materials, the shape [9] and mass of the isotensoid can be estimated.

VI. Trajectory Analysis

A key advantage of an IAD is its ability to increase the drag area ($C_D A$) earlier in the descent profile, enabling deceleration at higher altitudes vs the traditional DGB parachute. Additionally, the lack of a transonic drag bucket may permit the entry vehicle to release its heat shield at any point after IAD inflation without risking recontact. Early heat shield separation reduces the mass being decelerated and allows for onboard altimeters to acquire the ground sooner. This latter capability allows for the initiation of propulsive descent at a higher altitude, enabling landing at higher altitudes and/or providing more time to perform pinpoint landing guidance.

Trajectory simulations were performed using the program to optimize simulated trajectories (POST) [18]. The entry phase up to decelerator deployment employed the same reference bank-angle profile to be consistent with the DGB reference trajectory shown in Fig. 2. Three primary trades were evaluated: replacement of the nominal 23 m DGB with a supersonic IAD, replacement of the DGB with a two-stage IAD/ringsail combination, and the impact of an additional 20% increase in entry system mass.

A. Inflatable Aerodynamic Decelerator and Baseline Disk-Gap-Band System Comparison

This portion of the study investigates the system impact of increasing IAD diameters vs the present Astrobiology Field Laboratory baseline 23 m DGB parachute. Both IAD concepts are assessed. An initial comparison of the trajectories is provided in Fig. 10, in which IADs of varying diameters are shown deployed at the loft peak of the reference trajectory. Evident in Fig. 10 is the rapid, constant-altitude deceleration that occurs after IAD deployment. This is followed by transition to an asymptotic terminal descent in which drag and gravitational forces are nearly equal and opposite and the vehicle is descending on a line of constant dynamic pressure. Terminal velocity is strongly dependent on the diameter of the IAD, with diameters between 14 and 23 m shown in Fig. 10. Given that the terminal velocity represents the velocity at which the entry vehicle stages to propulsive terminal descent, a trade between IAD size and propellant mass arises. For example, a 14 m tension cone IAD provides a terminal velocity of 150 m/s at an altitude of 5 km, whereas a 20 m tension cone IAD provides a terminal velocity of 105 m/s at the same altitude. For reference, a 23 m DGB parachute deployed at Mach 2.3 results in a terminal velocity of 100 m/s at a 5 km altitude. Clearly, a larger IAD reduces the velocity and, thus, the propellant required for terminal descent, though at the expense of a heavier IAD system.

Figure 10 demonstrates that a significant increase in altitude (approximately 3 km) at subsonic velocities is possible with use of an IAD. Architecturally, this altitude increase can be used to provide either an increase in the terminal descent time line or the ability to land at higher surface elevations. However, this advantage belies the greater impact that an IAD can provide as a result of its large deployment condition envelope. That is, the DGB reference trajectory places the loft peak at a Mach number of about 3.3 and dynamic pressure of 1.5 kPa, whereas a supersonic IAD is capable of deploying at higher Mach numbers and greater dynamic pressures. Thus, a more suitable comparison can be made when the loft is repositioned. Retaining the reference bank profile, this is accomplished by entering at a shallower flight-path angle. For a relative entry flight-path angle of approximately −13.7 deg, the loft

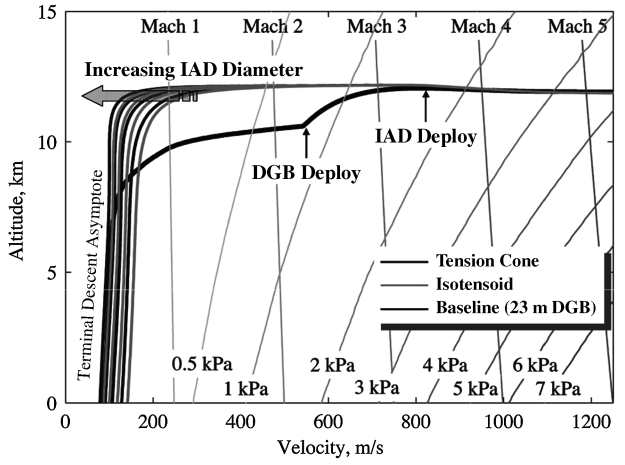

Fig. 10 Comparison of the reference trajectory and IAD modified trajectories with contours of Mach and dynamic pressure ($\gamma_{\text{entry}} = -16.1$ deg).

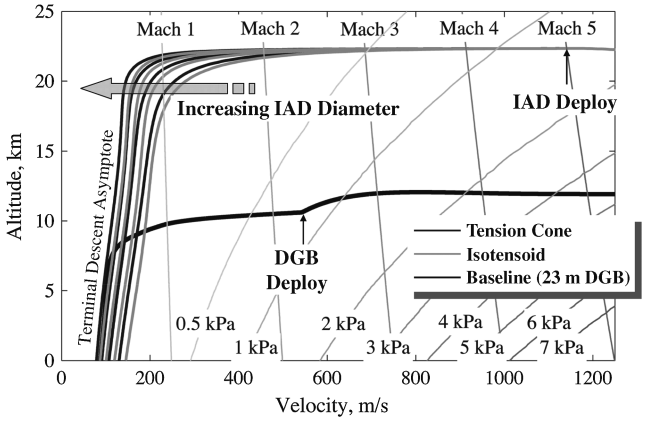

Fig. 11 Trajectory comparison for IAD modified trajectory with repositioned loft peak ($\gamma_{\text{entry}} = -13.7$ deg).

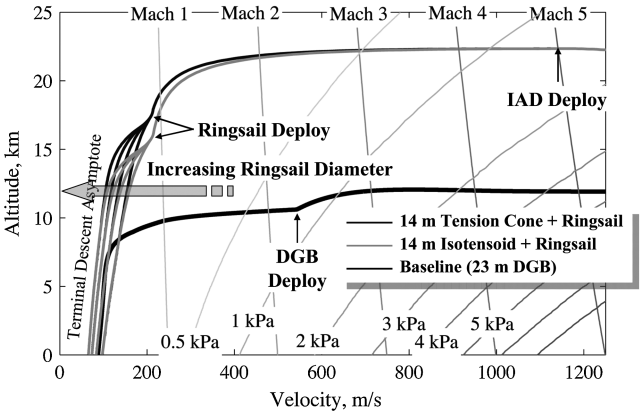

Fig. 13 Hybrid trajectory comparison for various ringsail diameters ($g_{\text{entry}} = -13.7$ deg).

peak occurs at Mach 5 and at a dynamic pressure nearly equivalent to before. The resulting trajectories are shown in Fig. 11.

Of note is that even moderately (14-m-diam) sized IADs can be used to attain subsonic velocities at altitudes nearly 10 km higher than the baseline DGB trajectory. The improved drag performance of the tension cone provides additional, but modest, advantages in altitude over the isotensoid design.

Although these trajectories do not represent optimized bank profiles, they still demonstrate the expanded entry, descent, and landing (EDL) system performance range that an IAD enables. If a steeper entry is desired, IADs can still provide a considerable altitude advantage. An example of this scenario is provided in Fig. 12, in which the bank profile was adjusted to provide more lift throughout the entry and the relative entry angle was steepened to −19 deg. This trajectory provides 8–10 km in increased altitude (as measured at the Mach 1 condition).

B. Inflatable Aerodynamic Decelerator and Two-Stage System Comparisons

The use of an IAD clearly provides significant flexibility in the terminal descent altitude and time line; however, a more massive IAD is required to achieve the same terminal velocity as a DGB parachute. Coupling a smaller IAD with a subsonic ringsail parachute would simultaneously allow for a lower terminal velocity, a lower IAD mass, and an increase in landed altitude. Although adding a second aerodynamic decelerator adds complexity to the EDL sequence of events, there could be significant mass savings that may act as a mission enabler. This portion of the study is performed with a 14 m IAD coupled with a ringsail parachute with diameters between 20 and 29 m. Ringsail deployment is assumed to occur at Mach 0.9. The results of this trajectory analysis are shown in Fig. 13.

Figure 13 shows a difference between the tension cone and isotensoid ringsail deployment altitude, which is expected due to the difference in the drag coefficient of the two configurations. The two IAD trajectories eventually converge to the same terminal velocity given similar ringsail parachutes. With the addition of the subsonic ringsail parachute, transitioning to propulsive descent at altitudes below 10 km does not require the improved drag performance of the tension cone. Lastly, the higher drag coefficient of a ringsail parachute provides for a moderate decrease in terminal velocity vs an equivalent-diameter DGB.

C. Entry Mass Sensitivity

To investigate the sensitivity of the inflatable decelerator and hybrid systems to increasing mass, two tension cone configurations were analyzed with two entry vehicle masses: the baseline 4.2 t vehicle and a roughly 20% heavier 5 t vehicle. The 5 t entry mass corresponds to achieving the packing density of the Mars exploration rover (MER) vehicles within the larger 4.5-m-diam aeroshell. The results of this trajectory analysis are shown in Fig. 14.

Figure 14 shows that an increase in mass acts to lower the altitude of the loft maneuver by about 2 km and, thus, lower the altitude of all subsequent EDL events. Although a decrease in altitude is undesirable, it illustrates that the tension cone is robust to entry system mass growth and still provides a significant altitude benefit vs the lower-mass baseline DGB system. In addition, Fig. 15 demonstrates that the two-stage 14 m tension cone IAD and ringsail system can deliver 20% more mass to approximately the same terminal velocity as the 23 m DGB reference mission.

Figure 15 shows that both the tension cone and the two-stage systems undergo about a 5 km decrease in propulsive staging altitude for a 20% increase in entry mass. However, this decrease in altitude

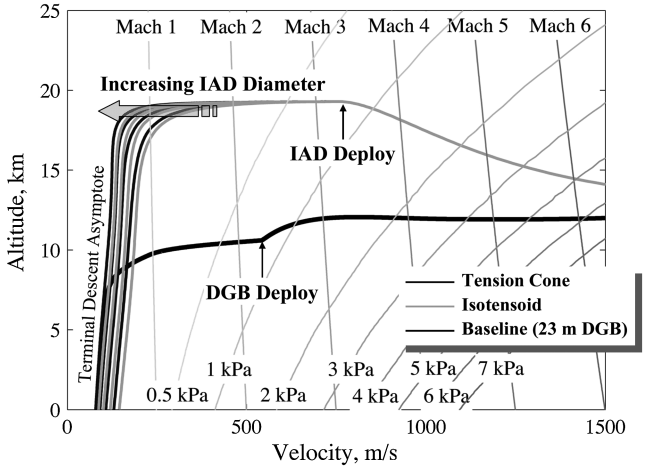

Fig. 12 Trajectory comparison for steepened, lift-up entry ($\gamma_{\text{entry}} = -19$ deg).

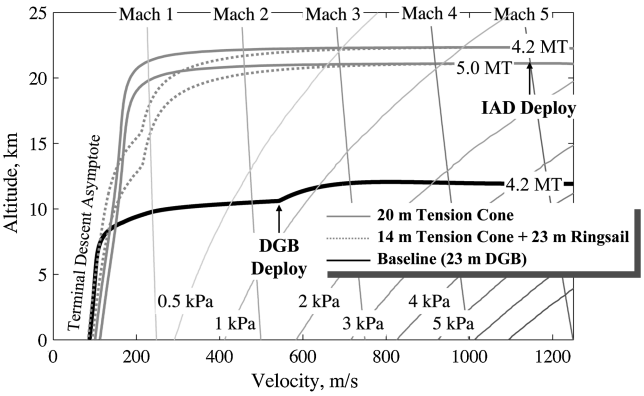

Fig. 14 Trajectory comparison for two entry system masses ($\gamma_{\text{entry}} = -13.7$ deg).

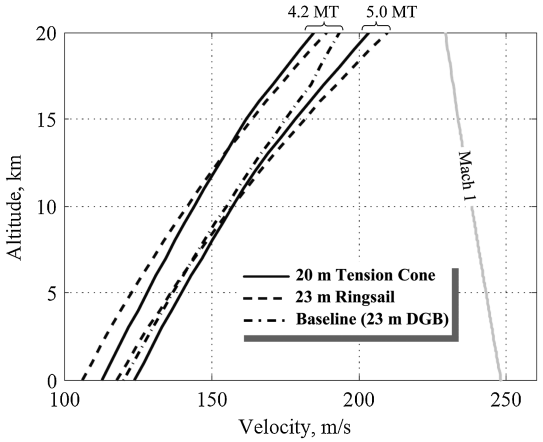

Fig. 15 Staging altitudes for varying entry vehicle masses.

does not endanger the mission for staging velocities above 125 m/s. This staging velocity could be further reduced by using a larger-diameter IAD or ringsail parachute as the baseline.

VII. Mass Estimates

The aerodynamic and trajectory benefits of an IAD are evident, but the ultimate measure of its viability must include an assessment of the additional mass that an IAD contributes to the EDL system and can deliver to the surface. Mass estimates were obtained for all aerodynamic decelerators (parachutes and IADs) based on fundamental structural principles and historical regressions (where data were available). For both IAD configurations, the fabric or film portions of the decelerator were sized assuming the material properties of Vectran™ fiber. Vectran™ fiber was selected based on its high strength-to-weight ratio, good thermal performance, and heritage on the Pathfinder and MER airbags. The same 200-denier Vectran™ material [19] used on the two MER landers was used in this study. This material has an areal mass density (ρ) of 0.0915 kg/m^2 and a tensile strength (σ_T) of 84, 940 N/m. The torus portion of the tension cone was assumed to have a higher areal density of 0.1458 kg/m^2 to account for the addition of a silicone coating used to reduce porosity. The final areal density used in the mass calculations was scaled linearly with the required tensile strength of the material.

A. Tension Cone Mass Estimation

The mass for the tension cone was determined as a summation of four different elements: the tension shell, the torus, the inflation gas, and the inflation system. The mass of the torus and the tension shell are derived from the density of the material used, the surface area, and the required material thickness:

$$m_{\text{ts}} = A_{\text{ts}}\rho_{\text{ts}}t_{\text{ts}} \tag{17}$$

$$m_t = A_t\rho_t t_t \tag{18}$$

where A is the surface area, ρ is the material density, t is the material thickness, and the subscripts t and ts represent the torus and tension shell, respectively. The minimum thickness can be calculated by comparing the material constraints with the various modes of failure detailed in Sec. IV. In particular, the thickness of the tension shell and torus can be estimated from Eqs. (2) and (3), respectively. These equations provide the required multipliers (c_{ts} and c_t) of nominal material thickness discussed in Sec. V.A. For a coated fabric torus, the limiting case is the circumferential stress, though the required antiwrinkling pressure and the compressive meridional stress levels are within the same magnitude. For this limit, the important parameters are the required inflation pressure, the major radius of the torus, and the torus thickness. It should be noted that the mass estimates neglect detailed elements, such as the mass of the seams, that would be particular to a given construction method.

The mass of the inflation gas (m_{gas}) is calculated using the ideal gas law:

$$m_{\text{gas}} = p_t V_t / RT \tag{19}$$

where p_t is the internal torus pressure, V_t is the torus volume, R is the gas constant of the fill gas, and T is the temperature of the fill gas (assumed to be 500 K). The volume of the torus is known from geometry. Using previously detailed failure criteria, the required inflation pressure can be determined. No accommodation was made in this mass estimation for pressurant gas leakage due to IAD porosity.

Both a tank system and a gas generator were investigated for the inflation system. Following the tank sizing guidelines in [20], the tank mass was estimated to be moderately higher than the mass of the inflation gas itself. Gas generators, on the other hand, typically yield much more favorable mass fractions. For this study, an inflation gas mass to total gas generator mass percentage of 75% was assumed.

Given the number of variables that are required to define a specific tension cone geometry, it is important to understand the impact that each has on the mass and performance of the system. With this in mind, an exploration of the tension cone design space was undertaken. Unless otherwise stated, the aeroshell diameter and area ratio, defined as

$$\text{AR} = (r_{\text{ts}} + r_t)^2 / r_a^2 \tag{20}$$

were kept constant using the values outlined in Table 2, whereas the ratio of r_{ts} to r_t and the tension cone angle (θ_{tc}) were varied. The dynamic pressure at deployment, important for torus pressure and tension shell loading concerns, was kept fixed at a value of 1400 Pa. The primary measure of effectiveness was mass, along with the required inflation pressure p_t, and a decelerator ballistic coefficient, defined as

$$\beta = \frac{(m_{\text{ts}} + m_t + \frac{4}{3}m_{\text{gas}})q}{D_{\text{tot}}} \tag{21}$$

The effect of θ_{tc} and the ratio of r_{ts} to r_t on the system mass can be seen in Fig. 16.

The mass is seen to vary greatly with θ_{tc} but is not strongly influenced by the ratio of r_{ts} to r_t except at the lower ratios. As the tension cone angle increases, the geometry becomes flatter, the drag increases, and the loading on the shell and torus increase as a result. Thus, the mass needed to withstand the added stresses increases. Increasing the ratio of r_{ts} to r_t also increases the mass, but at a much lower rate. This is less intuitive, as an increase in the ratio should yield a smaller torus and less surface area. However, the decrease in torus radius drives an increase in the required inflation pressure

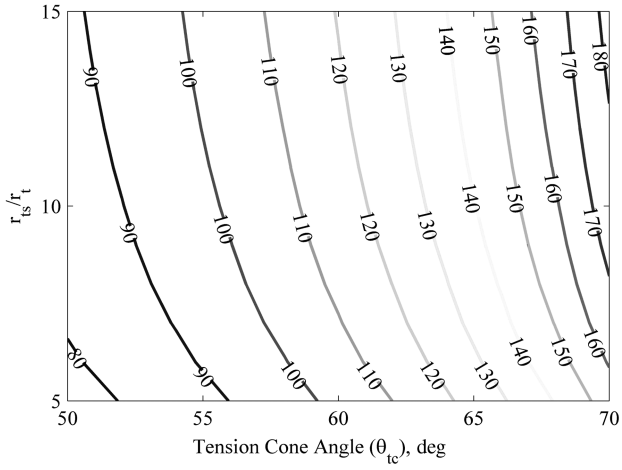

Fig. 16 Mass (kg) as a function of r_b/r_t ratio and interface angle.

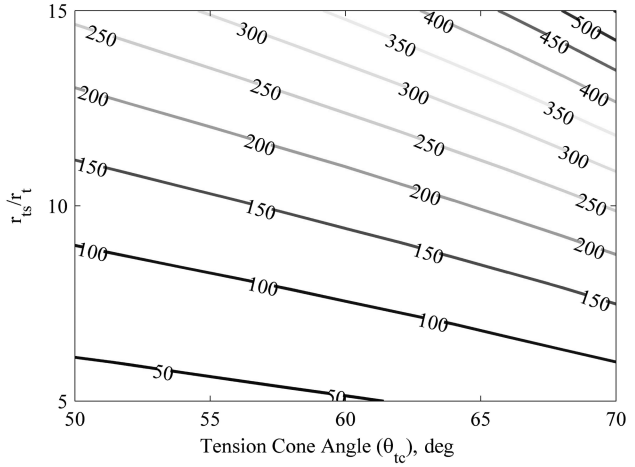

Fig. 17 Inflation pressure (kPa) as a function of the r_{ts}/r_t ratio and tension cone angle.

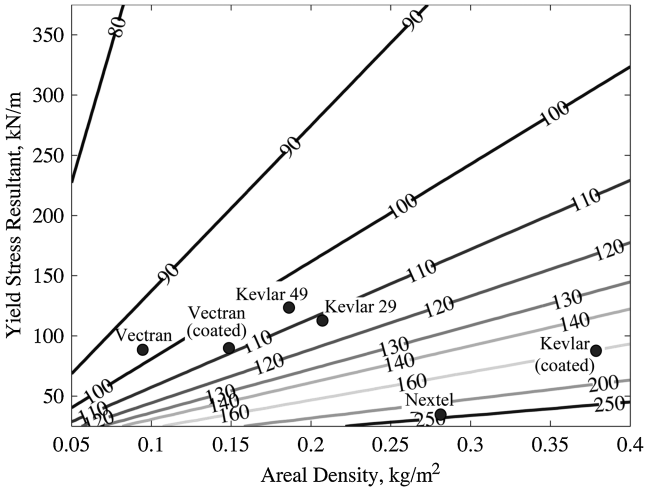

Fig. 19 Mass (kg) as a function of yield strength and material density.

needed to resist local surface wrinkling. This pressure increase rises more rapidly than the decrease in volume for a smaller torus. As a result, the net inflation gas mass rises. Furthermore, higher torus pressures increase the stresses on the torus and require thicker fabrics, thus raising the areal density of the material. For the material properties assumed, the inflation gas mass is shown to increase more rapidly than any decrease in material mass achieved by going to a smaller torus. The discussed change in internal pressure can be seen in Fig. 17. Again, decreasing the torus radius and, thus, increasing r_{ts}/r_t increases the pressure required to resist local wrinkling on the surface of the torus. Additionally, moving to larger tension cone angles increases drag and, thus, loading on the torus, with the results being a further increase in the required torus inflation pressure.

A secondary effect of changing the r_{ts}/r_t ratio or the tension cone angle is a change in drag performance. For a fixed total diameter, increasing r_{ts}/r_t decreases the shoulder radius and increases the drag coefficient. Likewise, decreasing the tension cone angle generates a more swept back decelerator and, consequently, reduces the drag coefficient. Thus, the two trends that reduce mass, namely, decreasing r_{ts}/r_t and the tension cone angle, also have the effect of reducing the drag performance of the tension cone. For this reason, it is useful to examine the impact that these two variables have on the decelerator ballistic coefficient defined by Eq. (21), a metric that includes both mass and drag performance. The results from this analysis are provided in Fig. 18. The key result is that the ballistic coefficient follows nearly the same trend as mass, indicating that the change in aerodynamics is a secondary effect.

Another important sensitivity addressed was the properties of the materials used for construction. For the level of fidelity of this study, these are the yield stress and areal density of the fabric. The effects of varying these can be seen in Fig. 19.

Based upon the results of the geometry parameter sweep, a tension cone angle of 60 deg and an r_{ts}/r_t ratio of 7 were selected as nominal values for subsequent sizing efforts. Though not optimal, the selected tension cone angle ensures a sufficient margin against the embedded shocks mentioned in Sec. III. The selected radius ratio ensures a lower mass while still providing good drag performance and lower torus volumes.

The trajectory analysis focused on IAD diameters of 14, 17, 20, and 23 m. Mass estimates for tension cones of these sizes are provided in Table 4. The results in Table 4 demonstrate that the total tension cone mass increases rapidly with increasing diameter. Furthermore, the rate of mass increase is larger than the rate of increase in the square of the total diameter. In other words, larger tension cones can be seen to yield larger decelerator ballistic coefficients.

The largest contributor to the rapidly increasing mass is the inflation gas, which, in turn, is driven primarily by torus pressure requirements. Of the five torus design constraints identified in Sec. V.A, it is the desire to eliminate localized wrinkling along the torus surface that affects the total mass the greatest. Should the assumption of membrane torus behavior be relaxed and the ability of the torus to resist wrinkling be improved through the addition of stiffness, the internal pressure can be reduced and dramatic improvements in total mass can be attained. This effect is shown in

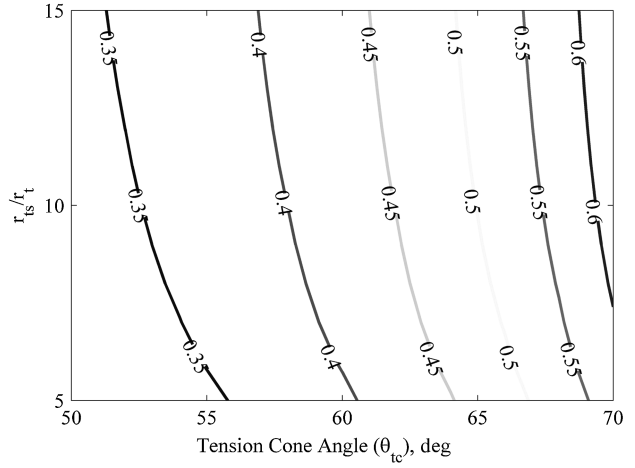

Fig. 18 Decelerator ballistic coefficient (kg/m^2) as a function of the r_{ts}/r_t ratio and tension cone angle.

Table 4 Tension cone mass for a range of diameters

IAD diameter		14	17	20	23
Geometry, m					
Tension shell radius	r_{ts}	6.125	7.438	8.750	10.063
Torus radius	r_t	0.875	1.063	1.250	1.438
Aeroshell radius	r_a	2.25	2.25	2.25	2.25
Mass, kg					
Tension shell	m_{ts}	2.3	5.4	11.0	19.8
Torus	m_t	29.7	55.3	92.1	142.0
Inflation gas	m_g	53.8	100.2	166.9	257.3
Gas generator		17.9	33.4	55.6	85.8
Total mass, kg	m_{tc}	104	194	326	505

Table 5 Tension cone mass with adjusted internal pressure constraints

IAD diameter, m	14	17	20	23
Total mass, kg				
100% inflation pressure	104	194	326	505
75% inflation pressure	78	147	247	384
50% inflation pressure	53	100	168	262

Table 5, in which total tension cone masses are shown vs reduced inflation pressure requirements.

From Table 5, it can be seen that a 50% reduction in inflation pressure requirements provides a nearly equivalent reduction in the total tension cone mass. Reducing the inflation pressure not only reduces the inflation gas mass, but also reduces the gas generator mass and the torus mass, the latter because of the reduced stresses on the torus.

B. Isotensoid Mass Estimation

The isotensoid mass essentially consists of two components that can be summed together: the meridional cord mass and the canopy fabric mass (assuming the canopy and burble fence are constructed of the same material). Thus, the mass of the isotensoid IAD can be represented as Eq. (22) [21]:

$$m_{\text{iso}} = n l_{\text{iso}} \Gamma + \rho A \tag{22}$$

where m_{iso} is the mass of the system, n is the number of meridional cords (assumed to be 48) of length l_{iso} with mass per unit length Γ, ρ is the material mass per unit area, and A is the total canopy surface area (including the burble fence). Given a desired shape, appropriate materials can be selected to satisfy the maximum fabric (f_f) and meridian stresses (T_f) required to obtain that shape.

To estimate the meridional cord mass, a factor of safety of 5 ($k_m = 5$) is applied to actual meridian tension (T_{act}) to obtain the design tension (T_{design}). Given the tensile strength of Vectran™, a meridian width (w_m) and, subsequently, a mass per unit length (m') is determined from Eq. (22). This mass per unit length is then used in Eq. (20) to obtain a total meridian mass.

$$T_{\text{design}} = k_m T_{\text{act}} \tag{23}$$

$$w_m = T_{\text{design}} / \sigma_T \tag{24}$$

$$m' = \rho w_m \tag{25}$$

For the canopy fabric, a similar factor of safety of 5 ($k_c = 5$) is applied to the actual stress resultant to obtain a design stress resultant. The primary constraint considered is that the design stress resultant be less than the tensile strength ($\sigma_{\text{design}} \leq \sigma_T$).

A summary of the mass estimation efforts for the isotensoid is provided in Table 6. When compared with the tension cone, the isotensoid is estimated as having a lower mass for a given diameter. Much of this can be attributed to the ram-air inflation mechanism of the isotensoid that eliminates the requirement for an independent inflation system. That is, even though the isotensoid configuration has significantly greater material acreage, the increase in material mass is still less than the mass of an inflation system. From a mass perspective, should it be possible to reduce the inflation pressure requirement of the tension cone torus, the two concepts would become much more equivalent. Lastly, as with the tension cone, the isotensoid can be seen to increase in mass more rapidly than the corresponding increase in drag area. However, this increase is at a lower rate than for the tension cone IAD and, in general, shows that the isotensoid scales better than the tension cone with regards to mass. A caveat to these results should be noted due to the lack of historical precedence in the manufacturing of IADs at these scales. This applies equally to both the tension cone and isotensoid mass estimates.

Table 6 Isotensoid mass for a range of diameters

IAD diameter, m		14	17	20	23
Meridians					
Cord length, m	l_m	15.7	20.7	24.5	28.7
Actual load, N	T_{act}	3187	4933	7152	9680
Width, m	w_m	0.19	0.29	0.42	0.57
Meridian mass, kg	m_m	13.0	26.4	45.4	71.8
Canopy					
Actual stress, N/m	σ_{act}	1080	1080	1077	1077
Surface area, m^2	A_f	403	617	842	1112
Canopy mass, kg	m_c	36.9	56.5	77.1	101.8
Total mass, kg	m_{iso}	50	83	122	174

C. Parachute Mass Estimation

The mass of the subsonic parachute system was estimated using a regression on historical ringsail system masses, resulting in the following mass estimating relationship:

$$m_p / A = 0.1055 \text{ kg/m}^2 \tag{26}$$

where m_p is the parachute mass and A is the parachute nominal area. The mortar mass required to eject a given parachute was similarly estimated from a linear regression of historical data, shown in Fig. 20.

D. Mass Estimate Summary

A summary of the mass estimates for each decelerator combination is provided in Table 7. Of note, the smaller IADs are shown to be mass competitive with the baseline 23 m DGB parachute.

The examination of mass estimates alone does not adequately portray the system view. Rather, the mass contributions must be weighed against other benefits that the IAD may provide. In particular, the trajectory benefits discussed in earlier sections must also be considered. One approach is to consider the velocity and altitude at which the decelerator system is staged to a propulsive terminal descent system. With this approach, a mission designer can effectively say, "How large of a system do I need to achieve a specific altitude and velocity combination for staging purposes, and what is the mass contribution of that system?" The following paragraphs outline the approach to and results from this type of analysis.

Each decelerator system is assessed based on two metrics: the *delta* mass (Δm_{sys}) of the deceleration system (both aerodynamic and propulsive) and the altitude at which propulsive descent was initiated. The delta mass represents the change in the decelerator system mass from the baseline that is incurred as a result of moving to an IAD or IAD/parachute two-stage system. This delta includes the mass of the decelerator system and any additional propellant required as a result of staging at a higher velocity. The value of the delta mass is the difference between the combined IAD/ringsail/propellant mass and the baseline DGB mass.

Five velocity conditions ranging from 200 to 100 m/s (propulsive descent is initiated at 110 m/s in the DGB reference trajectory) were selected to initiate propulsive descent. The altitude at which these velocity conditions are achieved will depend on the size of the IAD or parachute. Because mass is a function of size (i.e., diameter), the propulsive staging altitude is directly correlated to the IAD and parachute mass. The propellant mass required to null the remaining vehicle velocity is calculated via the rocket equation:

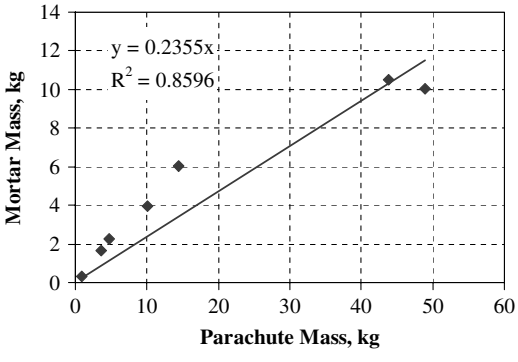

Fig. 20 Mortar mass vs parachute mass regression.

Table 7 Mass summary of decelerator systems

System configuration	Diameter, m	IAD[a]	Mass parachute[b], kg	Total
Baseline DGB	23	——	77	77
Tension cone	14	104	——	104
	17	194	——	194
	20	326	——	326
	23	505	——	505
Isotensoid	14	50	——	50
	17	83	——	83
	20	122	——	122
	23	174	——	174
Tension cone + Ringsail	14/20	104	41	145
	14/23	104	54	158
	14/26	104	69	173
	14/29	104	86	190
Isotensoid + Ringsail	14/20	50	41	91
	14/23	50	54	104
	14/26	50	69	119
	14/29	50	86	136

[a]IAD mass includes inflation system for tension cone
[b]Parachute mass includes mortar mass

$$m_{\text{prop}} = m_i[1 - \exp(-\Delta V / g_0 I_{\text{sp}})] \tag{27}$$

where m_i is the initial vehicle mass, m_f is the final vehicle mass, m_{prop} is the propellant mass, ΔV is the required change in velocity, g_0 is the acceleration due to the gravity of Earth ($g_0 = 9.81$ m/s^2), and I_{sp} is the specific impulse of the descent rocket engines, assumed to be 205 s based on the Viking terminal descent engines.

A summary of the delta propellant and delta system masses for each terminal velocity condition is provided in Table 8, in which it can be seen that nearly all configurations analyzed incurred mass increases over the baseline DGB system. However, the altitude at which propulsive descent can be initiated is significantly higher than the baseline configuration. For example, using a 20 m isotensoid IAD and staging at 175 m/s will incur a 150 kg increase in decelerator system mass but will also yield a 10 km increase in staging altitude. Lower staging velocities yield lower system mass increases, though at the expense of a smaller improvement in staging altitude. For example, using the same 20 m isotensoid and staging at 150 m/s provides only a 3 km increase in staging altitude. This is due to the IAD having reached its terminal descent slope [22]. In general, higher altitudes can be achieved by staging at higher velocities. Two-stage systems that include a subsonic ringsail parachute are shown to incur lower mass increases than the single IAD system, though typically with less altitude benefit. The most favorable situation for a two-stage system is shown to be for lower propulsive staging velocities. For example, a 14 m isotensoid coupled with a 29 m ringsail can provide a nearly 6 km altitude increase at a staging velocity of 100 m/s while only incurring a modest 43 kg increase in system mass.

The intent of Table 8 is to provide a mission designer with insight into the trades available for using IADs and how they may impact the descent profile. The use of a single IAD system can yield significant altitude increases so long as the vehicle is designed to stage at higher terminal descent velocities. Staging at higher altitudes and velocities is desirable as it affords the ability to mitigate navigation errors through terrain-relative navigation and guidance, allows an additional time line margin for subsequent descent and landing events, and allows for landing at higher-elevation sites.

Although Table 8 clearly shows altitude and trajectory advantages that can be attained from a supersonic IAD, it should also be recognized that an increase in payload mass is also attainable. Because a supersonic IAD is reasonably insensitive to increases in entry mass (Fig. 14), the IAD can accommodate an entry mass increase greater than the mass of the IAD itself. For example, an entry mass of 5 t can be decelerated to subsonic velocities at nearly the same altitude as a 4.2 t entry mass. Because the IAD system would constitute significantly less than the 800 kg increase in mass, the net effect is an increase in payload mass. With this in mind, the mass

Table 8 System study metric summary for 4.2 t baseline case

Staging velocity, m/s		200		175		150		125		100	
Δm_{prop}, kg		143		104		65		24		−16	
Configuration	Diameter, m	Staging alt., km	Δm_{svs}, kg	Staging alt., km	Δm_{sys}, kg	Staging alt., km	Δm_{sys}, kg	Staging alt., km	Δm_{sys}, kg	Staging alt., km	Δm_{sys}, kg
Baseline DGB	23	9.4	——	9.1	——	8.7	——	8.1	——	4.5	——
Tension cone	14	15.9	170	10.1	131	4.7	92	——	——	——	——
	17	19.9	260	17.4	221	10.4	182	4.5	141	——	——
	20	21.1	392	20.3	353	16.9	314	9.0	273	2.8	233
	23	21.6	571	21.2	532	20.3	493	13.0	452	6.6	412
Isotensoid	14	13.0	116	6.3	77	1.0	37	——	——	——	——
	17	18.8	149	12.9	110	6.7	70	1.3	30	——	——
	20	20.7	189	19.1	150	11.7	110	5.9	70	0.1	29
	23	21.4	240	20.8	201	18.0	161	9.7	121	3.9	80
Tension cone+ ringsail	14/20	15.6	211	13.8	172	10.8	133	6.3	92	0.6	52
	14/23	15.9	224	14.8	185	13.2	146	10.1	105	4.7	65
	14/26	15.9	239	15.2	200	14.2	161	12.4	120	7.9	80
	14/29	15.9	256	15.2	217	14.6	178	13.6	137	10.7	97
Isotensoid + ringsail	14/20	14.0	157	12.5	118	10.2	78	6.3	38	0.7	−2
	14/23	14.2	170	13.3	131	11.9	92	9.6	51	4.7	11
	14/26	14.2	185	13.6	146	12.7	107	11.3	66	7.9	26
	14/29	14.2	202	13.6	163	13.0	123	12.1	83	10.2	43

Table 9 Payload increases possible for a 5 t entry mass using various IAD configurations

Staging velocity, m/s		200		175		150		125		100	
Δm_{prop}, kg		143		104		65		24		−16	
Configuration	Diam., m	Stage alt., km	Δm_{pl}, kg	Stage alt., km	Δm_{pl}, kg	Stage alt., km	Δm_{pl}, kg	Stage alt., km	Δm_{pl}, kg	Stage alt., km	Δm_{pl}, kg
Tension cone	14	12.7	587	7.0	638	1.7	689	——	——	——	——
	17	17.9	497	14.2	548	7.5	599	1.5	651	——	——
	20	19.6	365	18.5	416	13.0	467	6.2	519	——	——
	23	20.2	186	19.8	237	18.4	288	10.1	340	3.8	393
Isotensoid	14	9.4	641	3.2	692	——	——	——	——	——	——
	17	16.5	608	9.5	659	3.8	710	——	——	——	——
	20	19.0	568	16.4	619	8.7	671	3.1	723	——	——
	23	20.0	517	19.1	568	13.9	620	7.0	672	0.9	725
Tension cone + ringsail	14/20	15.1	546	12.6	597	8.4	648	3.5	700	——	——
	14/23	15.5	533	14.2	584	12.0	635	7.5	687	1.7	740
	14/26	15.6	518	14.8	569	13.6	620	10.8	672	5.2	725
	14/29	15.6	501	15.0	552	14.2	603	12.7	655	8.2	708
Isotensoid + ringsail	14/20	13.6	600	11.6	651	8.3	702	3.5	755	——	——
	14/23	14.0	587	12.9	638	11.1	689	7.4	741	1.7	794
	14/26	14.1	572	13.4	622	12.3	674	10.2	726	5.2	779
	14/29	14.2	202	13.6	163	13.0	123	12.1	83	10.2	43

analysis performed for the 4.2 t entry case was also performed on a 5 t entry case. However, the previous metric of delta system mass has been replaced with a net increase in payload capability, corresponding to the difference between the increased entry mass and the mass of the IAD and additional propellant. The results from this trade are shown in Table 9. It should be mentioned that, in this context, the increased payload mass does not necessarily represent an equivalent increase in rover mass or landed mass. Rather, some of the payload increase will likely be consumed by increased structural masses, larger propellant tanks, etc., that result from an increased entry mass.

From Table 9 it can be seen that payload increases of 600 kg or more are attainable with the use of an IAD system. The greatest payload increases occur with smaller IADs. For example, using a 14 m isotensoid IAD and staging at 200 m/s can provide a 641 kg increase in payload mass at a staging altitude of over 9 km. The use of a parachute for this increased entry mass would require deployment at dynamic pressures of roughly 1 kPa, a full third beyond that planned for the MSL. Although it may theoretically be possible to develop a parachute that would work for these increased masses, doing so would likely require a costly qualification program, similar to the Balloon Launch Decelerator Test Program undertaken for the Viking missions. Given the marginal increase in payload mass that such a program would ultimately afford, it may be more prudent to spend those resources qualifying a supersonic IAD, a technology that would enable a greater range of entry masses for future Mars systems.

VIII. Conclusions

The objective of this system study was to show how the use of inflatable aerodynamic decelerators can provide a technology path to enable higher altitude and higher mass landing on the surface of Mars. Both a tension cone and isotensoid IAD configuration were investigated. As an aerodynamic database for such IADs does not exist, a preliminary database was constructed computationally using a Cartesian-grid flow solver. Trajectories using IADs and IAD/parachute two-stage systems were compared relative to a nominal trajectory using a traditional DGB parachute.

Results from this performance analysis demonstrated the IAD's ability to drastically improve the altitudes at which the entry vehicle transitions to subsonic velocities. Additional improvement was possible when the reference entry flight-path angle or entry bank-angle profile was adjusted to allow for IAD deployment at higher Mach numbers and altitudes.

Structural analyses, material properties, and historical regressions were used to generate mass estimates for the decelerator systems to provide a complete representation of each system. These preliminary mass estimates showed the isotensoid configuration to be a lower-mass solution, though much potential exists to improve the mass performance of the tension cone. Each of the decelerator systems were assessed based on two metrics: the mass of the IAD EDL system architecture relative to the reference DGB EDL system architecture and the altitude at which propulsive descent can be initiated for each system. Systems that incorporated only a single IAD were favorable at higher terminal propulsion staging velocities whereas systems that incorporated a two-stage IAD/parachute system were more favorable at lower staging velocities. Because of their significant insensitivity to increased entry masses, IADs can also increase payload mass considerably. Increasing the entry mass by 800 kg above the 4.2 t DGB EDL architecture provided an increase in payload mass of approximately 600 kg, particularly when using smaller IADs.

Acknowledgments

This work was funded by NASA Langley Research Center's Program to Advance Inflatable Decelerators for Atmospheric Entry. The authors would like to thank Juan R. Cruz of NASA Langley Research Center for his guidance on the structural aspects of IADs. We would also like to thank Jeff Tooley of the Jet Propulsion Laboratory for his assistance in developing the Mars 2016 entry trajectory model.

References

[1] Way, D. W., Powell, R. W., Chen, A., Stelzner, A. D., San Martin, A. M., Burkhart, P. D., and Mendeck G. F., "Mars Science Laboratory: Entry, Descent, and Landing System Performance," Institute of Electrical and Electronics Engineers Paper 1467, 2006.

[2] Braun, R. D., and Manning, R. M., "Mars Exploration Entry, Descent, and Landing Challenges," *Journal of Spacecraft and Rockets*, Vol. 44, No. 2, March–April 2007, pp. 310–323. doi:10.2514/1.25116

[3] Sengupta, A. et al. "Overview of the Mars Science Laboratory Parachute Decelerator System," AIAA Paper 2007-2578, May 2007.

[4] Cruz, J. R., and Lingard, J. S., "Aerodynamic Decelerators for Planetary Exploration: Past, Present, and Future," AIAA Paper 2006-6792, Aug. 2006.

[5] Anderson, M. S., Robinson, J. C., Bush, H. G., and Fralich, R. W., "A Tension Shell Structure for Application to Entry Vehicles," NASA TN D-2675, 1965.

[6] Barton, R. R., "Development of Attached Inflatable Decelerators for Supersonic Application," NASA CR-66613, 1968.

[7] Anon., "PEPP Ballute Design and Development Final Report," NASA CR-66585, 1967.

[8] Beegle, L. W., Wilson, M. G., Abillerira, F., Jordan, J. F., and Wilson, G. R., "A Concept for NASA's Mars 2016 Astrobiology Field Laboratory," *Astrobiology*, Vol. 7, No. 4, 2007, pp. 545–577.

doi:10.1089/ast.2007.0153
[9] Cruz, J. R., Cianciolo, A. D., Powel,l, R. W., Simonsen, L. C., and Tolson, R. H., "Entry, Descent, and Landing Technology Concept Trade Study for Increasing Payload Mass to the Surface of Mars," *4th International Symposium on Atmospheric Reentry Vehicles and Systems*, Association Aeronautique and Astronautique of France, March 2005.
[10] Houtz, N. E., "Optimization of Inflatable Drag Devices by Isotensoid Design," AIAA Paper 64-437, July 1964.
[11] Mikulas, M. M., Jr., and Bohon, H. L., "Development Status of Attached Inflatable Decelerators," *Journal of Spacecraft and Rockets*, Vol. 6, No. 6, June 1969, pp. 654–660. doi:10.2514/3.29636
[12] Bixby, H. W., Ewing, E. G., and Knacke, T. W., "Recovery Systems Design Guide," Air Force Flight Dynamics Laboratory TR-78-151, 1978.
[13] Deveikis, W. D., and Sawyer, J. W., "Aerodynamic Characteristics of Tension Shell Shapes at Mach 3.0," NASA TN D-3633, Oct. 1966.
[14] Lee, J., and Ruffin, S. M., "Parallel Computation of Solution Adaptive Cartesian Grids with SFC," AIAA Paper 2007-4088.
[15] Young, W. C., and Budynas, R. G., *Roark's Formulas for Stress and Strain*, 7th ed., McGraw–Hill, New York, 2001, p. 526.
[16] Kyser, A. C., "Deployment Mechanics for an Inflatable Tension-Cone Decelerator," NASA CR-929, 1967.
[17] Weeks, G. E., "Buckling of a Pressurized Toroidal Ring Under Uniform External Loading," NASA TN D-4124, 1967.
[18] Powell, R. W., Striepe, S. A., Desai, P. N., Braun, R. D., Brauer, G. L., Cornick, D. E., Olson, D. W., Peterson, F. M., and Stevenson, R., "Program to Optimize Simulated Trajectories (POST) Utilization Manual,"Vol. 2, Ver. 5.2, NASA Langley Research Center, Hampton, VA, 1997.
[19] Stein, J., and Sandy, C., "Recent Developments in Inflatable Airbag Impact Attenuation Systems for Mars Exploration," AIAA Paper 2003-1900, April 2003.
[20] Humble, R., Lewis, D., Bissel, W., and Sackheim, R., *Liquid Rocket Propulsion Systems*, 1st ed., McGraw–Hill, New York, 1995, pp. 272–279.
[21] Anderson, M. S., Bohon, H. L., and Mikulas, M. M., Jr., "A Structural Merit Function for Aerodynamic Decelerators," NASA TN D-5535, 1969.
[22] Way, D. W., Powell, R. W., Chen, A., and Stelzner, A. D., "Asymptotic Parachute Performance Study," Institute of Electrical and Electronics Engineers Paper 1465, 2006.

J. Martin
Associate Editor